Journal of Alloys and Compounds 698 (2017) 1094–1101

Contents lists available at ScienceDirect

Journal of Alloys and Compounds

journal homepage: http://www.elsevier.com/locate/jalcom

Erosion-wear and intergranular corrosion resistance properties of AISI 304L austenitic stainless steel after low-temperature plasma nitriding

Xujuan Qin [a, *], Xianglong Guo [b, **], Junqiang Lu [c, ***], Liangyu Chen [d], Jining Qin [a], Weijie Lu [a]

[a] State Key Laboratory of Metal Matrix Composites, Shanghai Jiao Tong University, Shanghai 200240, China
[b] School of Nuclear Science and Engineering, Shanghai Jiao Tong University, Shanghai 200240, China
[c] Shanghai Nuclear Engineering Research & Design Institute, No. 29 Hongcao Road, Shanghai 200233, China
[d] School of Mathematics and Science, Jiangsu University of Science and Technology, Zhenjiang, Jiangsu 212003, China

ARTICLE INFO

Article history:
Received 10 December 2015
Received in revised form
5 December 2016
Accepted 13 December 2016
Available online 20 December 2016

Keywords:
Austenitic stainless steel
Low-temperature plasma nitriding
Expanded austenitic phase
Erosion-wear
Intergranular corrosion

ABSTRACT

In this paper, AISI 304L austenitic stainless steel has been subjected to plasma nitriding at 673 and 681 K lasted for 6, 18, 24, and 36 h. The morphology, microhardness, phase, and microstructure evolution of the nitrided layer were studied. Not only an expanded austenitic phase (γ_N) but also Cr-nitrides were formed in the nitrided layer. Transmission Electron Microscopy (TEM) study showed the formation of amorphous and nanocrystalline phases in the surface layers of the samples. The erosion-wear and intergranular corrosion (IGC) resistance behaviors of the nitrided samples were studied in detail. As compared to the non-nitrided sample, the erosion-wear resistance of the nitrided layer at normal impact angle doubles after nitriding at 673 K for 6 h, as a result of the formation of γ_N phase. Degree of sensitization (DOS) of IGC is gradually enhanced with the increase of nitriding time as indicated by a double loop electrochemical potentiokinetic reactivation (DL-EPR) measurement. This is assigned to the nanostructuring and to the Cr-depletion in the areas adjacent to the Cr-nitrides.

1. Introduction

Austenitic stainless steels (ASS) have attracted much attention due to their good corrosion resistance [1]. However, the low hardness and poor wear resistance of ASS impede their widespread applications under corrosion conditions. Therefore, efforts should be made to enhance the mechanical and wear resistance properties of ASS. Among the various processes, low-temperature plasma nitriding is one of the most efficient and universal technologies for ASS, in which expanded austenitic phase (γ_N) with high hardness and good erosion-wear resistance on the surface can be formed [2–7]. However, intergranular corrosion (IGC) can destroy the binding force between the grain boundary and reduce the mechanical strength of the metal. In general, the intergranular attack on the stainless steel occurs at regions adjacent to chromium depletion, and is attributed to chromium precipitation and grain size refinement on the grain boundary through heat treatment [8,9]. Besides, the erosion-wear damage can increase significantly on the material surface under the impact of solid particles, which limits its service life [10]. Therefore, it is urgent to enhance the wear and corrosion resistance behaviors of ASS, which will broaden their applications.

Plasma nitriding can result in different kinds of precipitation and in the changes of microstructure on the surface, which has an influence on the erosion wear and IGC properties. The formation of Cr-nitrides layers contributes to an extreme increase of hardness and wear resistance on the surface of ASS, whereas it sacrifices the corrosion resistance [11]. Previous literatures have revealed that CrN does not precipitate under the condition of nitriding below 673 K [2,12,13]. However, the expanded austenite phase (γ_N) and CrN precipitates can be simultaneously formed inside the original grains when ASS are nitrided above 723 K [14,15]. The precipitation of Cr-nitrides results in the formation of chromium-depleted regions, which decreases the corrosion resistance of ASS [16]. After nitriding, the formation of nanocrystalline structures on the top layer of ASS can be related to the enhanced chemical reaction

* Corresponding author.
** Corresponding author.
*** Corresponding author.
E-mail addresses: qinxujuan0916@163.com (X. Qin), guoxianglong@sjtu.edu.cn (X. Guo), lujunqiang@snerdi.com.cn (J. Lu).

http://dx.doi.org/10.1016/j.jallcom.2016.12.164
0925-8388/

kinetics [17–20]. The formation of Cr-nitrides and other phases within the modified layer of ASS leads to an increase of erosion-wear resistance and decrease of corrosion resistance [21,22]. The erosion-wear resistance of the martensite on the nitrided layer is improved where γ_N and CrN are formed [23]. However, only a limited number of works on the erosion-wear and IGC of ASS under low-temperature nitriding were reported. Therefore, it is important to take a full consideration of both the erosion-wear resistance and IGC resistance of ASS after the low-temperature nitriding.

In this work, the process of plasma nitriding was controlled by means of the surface treatment on AISI 304L at different nitriding conditions. The thickness, microhardness, precipitated phases, and microstructure of the modified layer were investigated. Moreover, the erosion-wear resistance and IGC resistance behaviors of the nitrided samples after different nitriding processes were systematically studied.

2. Experimental

2.1. Materials

The chemical composition (wt %) of AISI 304L ASS is 0.03 C, 2 Mn, 0.01 P, 0.02 S, 0.05 Si, 0.05 Co, 10 Ni, 18 Cr, and Fe balance. The major parameters of the tubing samples are as follows: external diameter, 9.44 mm; inner diameter, 8.74 mm; surface roughness (R_a) $\leq$ 1.6 μm. Note that the size of the samples was measured from the last line of cold work after the annealing treatment. The cross-sectional cold deformation of the tested tubing samples is approximately 10%.

2.2. Nitriding process

The as-prepared samples were processed in a pulsed direct current (DC) glow discharge plasma nitriding furnace. To begin with, the samples were cleaned by glow discharge in a gas mixture of H_2 and Ar, where the vacuum was controlled below 50 Pa. The samples were then nitrided at different temperatures (673 and 681 K) and times (6, 18, 24, and 36 h). All the nitriding experiments were carried out in a gas mixture of 25% N_2 + 75% H_2 under the pressure of 300 Pa. After nitriding treatment, all samples were cooled to room temperature in vacuum.

2.3. Characterization

The samples for cross-section morphology were etched with a solution containing 50 vol % HCl + 25 vol % HNO_3 + 25 vol % H_2O for 60 s. The phase compositions of the samples were analyzed by X-ray powder diffraction (XRD) using a Rigaku Ultima IV X-ray diffractometer with Cu Kα radiation (λ = 1.5406 Å) at 40 kV and 30 mA. The microhardness on the surface was measured by a 402 SXV Knoop microhardness tester with loads of 25 g and a loading time of 10 s. The microhardness results are the average values from 10 measurements. The thin foils for TEM analysis were prepared by ion milling. TEM images and selected-area electron diffraction (SAED) patterns on the surface of the nitrided layer were carried out by JEOL-7600F.

2.4. Erosion-wear tests

The erosion-wear resistance of the nitrided samples was tested by a Palmeso Micro Slurry-jet Erosion Super (MSE-S) tester. Compressed air and slurry (a mixture of water and Al_2O_3 particles with the size of 1.6 μm) were blended in the spray nozzle, and then jetted to the sample surface at high speed, which produced a corresponding erosion trace. The process was carried out under the normal impact. The temperature during the test was kept at 293 K. The measurement transformed the wear loss into a wear ratio, followed by using the wear ratio to assess the strength of the material surface coating. Finally, the relation between the wear depth and the projected particle amount was obtained and the slope of the fitting curve was defined as the wear ratio.

2.5. DOS of IGC measurements

IGC of the nitrided samples was measured by the DL-EPR method, which was the universal route for evaluating the DOS of IGC. The DOS of the samples was tested in a solution of 0.5 M H_2SO_4 + 0.01 M KSCN, which was based on the ASTM G108 standard (JIS G 0580-1986) [24]. To determine the peak of activation current density (I_a), the samples were scanned from the value of corrosion potential to a passivation potential of +300 mV SCE at a scan rate of 1.67 mV/s. The applied potential was then reversed, and the sample was cathodically swept back to the initial potential to determine the peak of reactivation current density (I_r) [25]. The temperature was kept stable at 303 K. Platinum sheet and the saturated calomel electrode were used as counter and reference electrodes, respectively. The DOS of IGC is defined by the formula

$$R = \frac{I_r}{I_a} \times 100\%$$

where I_r is the peak of the reactivation current density and I_a is the peak of the activation current density. In general, the greater the R value, the worse the IGC resistance.

3. Results and discussion

3.1. Phase, morphology, and microhardness analysis

The cross-section morphology of a nitrided sample after etching at 673 K for 36 h is shown in Fig. 1. The nitrided layer with a thickness of about 11 μm (white region in Fig. 1) is clearly visible after etching. As listed in Table 1, the thickness of the nitride layer in AISI 304L ranges from 1 to 14 μm after nitriding at different times and temperatures. Amazingly, although the thickness of the nitrided layer does not reach 1 μm after 6 h nitriding at 673 K, the microhardness on the surface increases up to 4 times as compared to that of the substrate (280 HK). This is mainly attributed to the

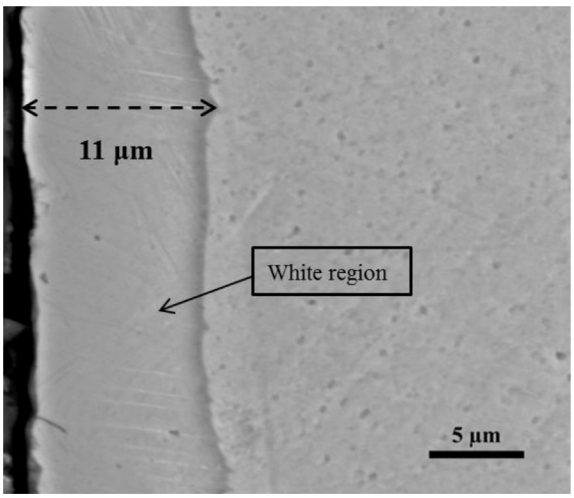

Fig. 1. The cross-section morphology of the nitrided layer formed at 673 K for 36 h.

Table 1
The thickness and surface microhardness of the treated samples obtained under different nitriding conditions.

Nitriding condition	Thickness (μm)	Microhardness (HK)
673 K -6 h	<1	1150
673 K -18 h	4	1250
673 K -24 h	10	1350
673 K -36 h	11	1600
681 K -18 h	14	1300

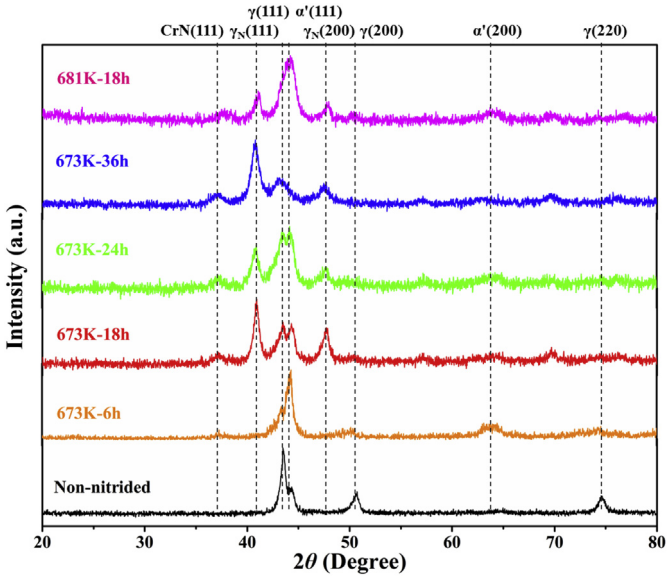

Fig. 2. The XRD patterns of the non-nitrided and nitrided samples under different conditions.

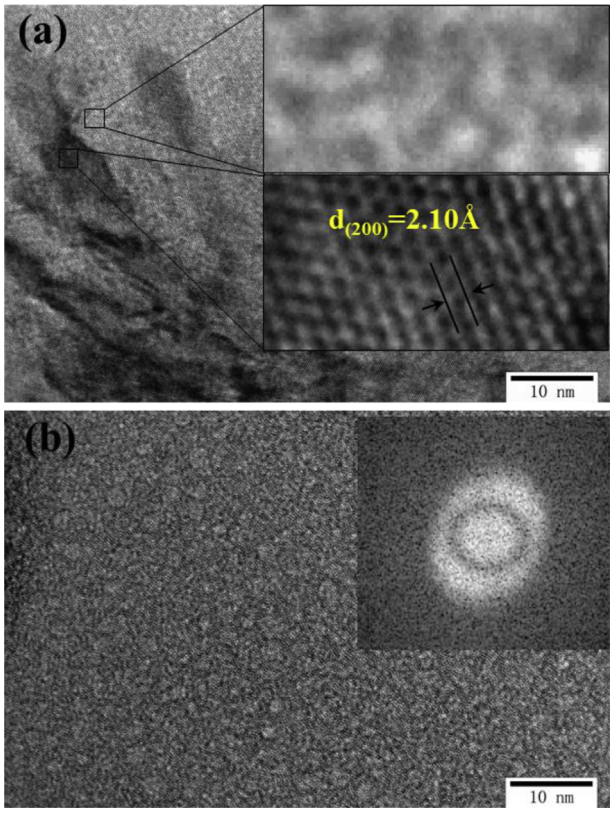

Fig. 4. HR-TEM images of the surface layer of the sample nitrided at 681 K for 18 h: (a) the morphology on the top surface and (b) the amorphous and nanocrystalline phases of the nitrided layer surface. The insets in (a) show the highly-magnified TEM images of γ_N (top) and CrN (bottom). The inset in (b) shows the SAED pattern of the amorphous phase.

formation of the expanded austenite because of accommodation of the N atoms into the interstitial sites [26].

As illustrated in Table 1, the thickness and surface microhardness of the nitrided layer are increased dramatically with the increase of the nitriding time from 6 h to 24 h at 673 K. The increase of the thickness of the nitrided layer reaches a limit when the nitriding time exceeds 24 h at 673 K, while the surface

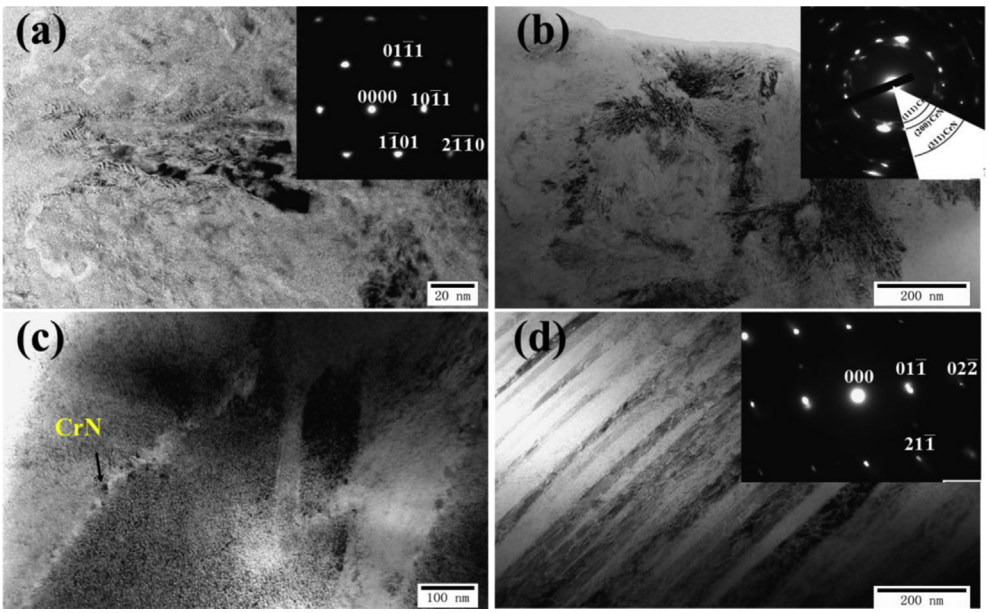

Fig. 3. TEM images of AISI 304L nitrided at 681 K for 18 h: (a) the morphology of the nitrided layer, (b) the region of the nitrided layer with lamellar (α + CrN) structure, (c) CrN precipitate on the nitrided layer, (d) the lath-shaped structure of the nitrided layer. The insets in (a), (b), and (d) show the corresponding SAED patterns.

microhardness of the nitrided layer increases sharply. This is because the nitrogen content becomes supersaturated in the surface layer when the nitriding time is over 24 h. This prevents further diffusion of nitrogen. When the nitriding time is fixed at 18 h, the thickness of the nitrided layer increases from 4 to 14 μm with the increase of the nitriding temperature from 673 to 681 K. The activity of N atoms increases with the increase of the nitriding temperature, resulting in the increase of nitrogen concentration at the surface of the nitrided layer [12]. In addition, Cr-nitrides are formed with the increase of the nitriding time, which is ascribed to the reaction between the enriched N and Cr at the grain boundary on the surface, resulting in a huge improvement of the microhardness on the surface.

Fig. 2 shows the XRD patterns of the non-nitrided and nitrided samples at different temperatures and times. The non-nitrided sample shows the diffraction peaks of γ-Fe phase and martensite α′ phase. A cold deformation by 10% of thin tubes in AISI 304 L leads to the formation of martensite α′. However, γ_N phase and a little amount of CrN are detected on the surface of the sample nitrided at 673 K for 6 h. With the increase of the nitriding time, the amount of

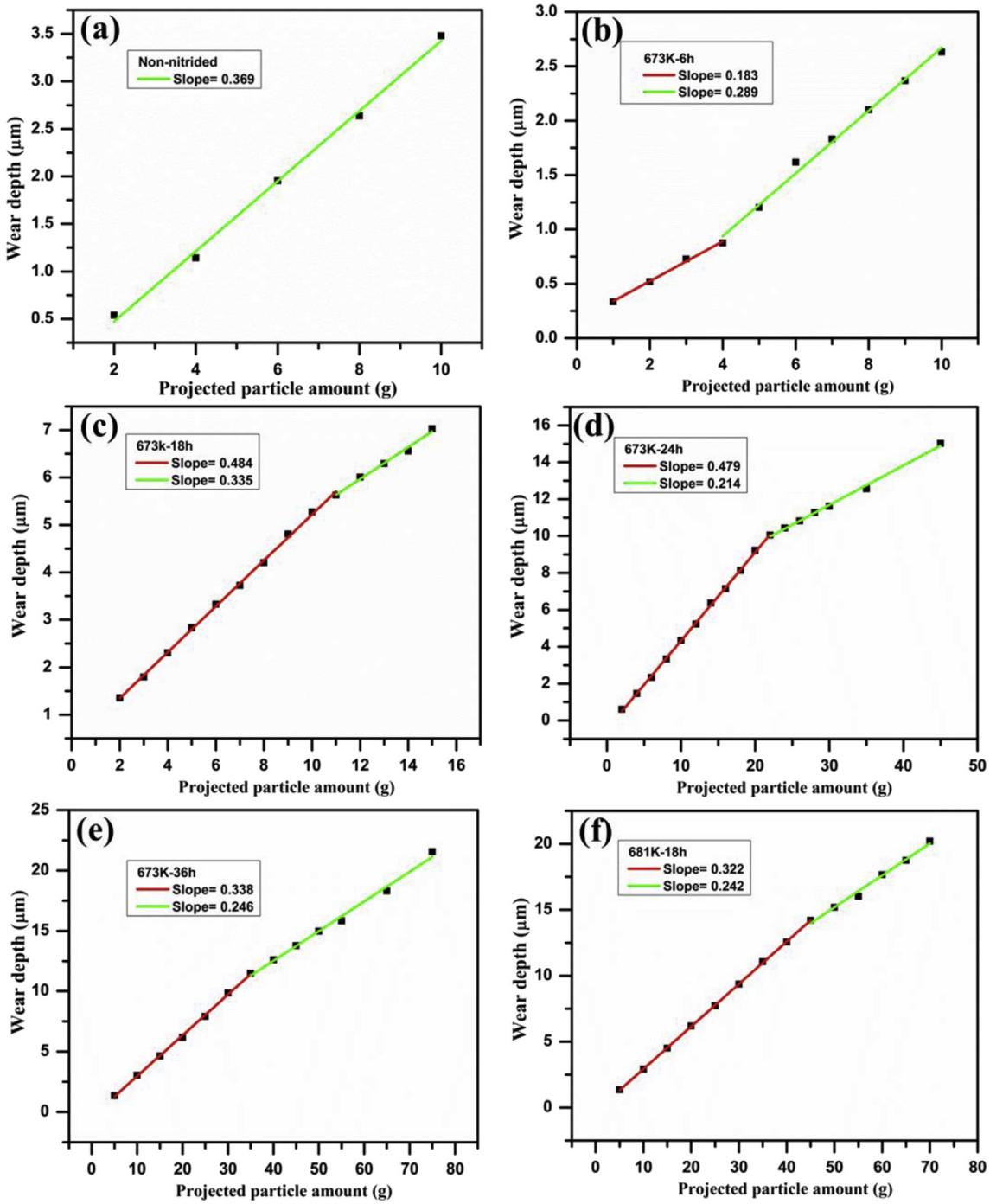

Fig. 5. Erosion-wear relation curves of the wear depths as a function of the rejected particle amounts under different treatments at normal impact condition. The erosion wear ratios of the substrate and the nitrided layer are represented by a green line and red line. (For interpretation of the references to colour in this figure legend, the reader is referred to the web version of this article.)

γ_N phase increases while that of γ-Fe phase decreases. In comparison to γ-Fe phase, the peaks of γ_N phase shift to the lower diffraction angles, which is related to the lattice expansion induced by the interstitial solid solution of nitrogen [3]. In addition, the diffraction peaks are broadened with increasing nitriding time, which results from the stresses and grain refinement [27,28]. This conclusion is supported by the TEM analysis. Based on the XRD results, it appears that the formation of γ_N is the major reason for the increase of microhardness. Besides, the formation of small amounts of CrN and nanocrystalline phases also contribute to the increase of the nitrided layer's microhardness.

To further investigate the microstructure of the nitrided samples, TEM analysis (Fig. 3) was carried out on the surface of the nitrided layer treated at 681 K for 18 h. Large amounts of diffuse crinkle and Cr_2N regions are visible in Fig. 3a. The formation of Cr_2N can be further verified by the SAED pattern (the inset in Fig. 3a). When the potential energy of the implanted nitrogen atoms reaches the diffusion potential barrier, the unceasingly introduced nitrogen cannot further diffuse into the substrate, which leads to nitrogen enrichment on the surface of the nitrided layer. The excessive nitrogen atoms react with Cr at the grain boundary and thereafter form Cr_2N in the top layer which is precipitated in situ [29]. In addition, the lamellar (α + CrN) structure is formed from the eutectoid transformation of the non-equilibrium γ_N [30], which is validated by the SAED pattern (the inset in Fig. 3b). Besides, nanoscale CrN (Fig. 3c) discontinuously precipitated at the grain boundaries. Fig. 3d shows the typical lath-shaped structure of α and CrN in the nitrided layer and the corresponding SAED pattern (the inset in Fig. 3d).

As shown in Fig. 4, nanocrystalline and amorphous phase constituents are present on the surface. The observed nanocrystalline component is a recrystallized structure resulting from the eutectoid transformation of $\gamma_N \rightarrow \alpha + CrN$ with the increase of the nitriding time. As shown in Fig. 4a, nanoscale CrN is diffusely distributed in the regions of γ_N phase. The boundaries between them are clearly visible. The interplanar distance between {200} CrN is measured to be 2.10 Å. The implanted N atoms occupy the interstitial sites of the fcc 304L, resulting in severe lattice expansion (the insets in Fig. 4a). Fig. 4b shows the amorphous phase produced by plasma nitriding, on which is scattered the nanocrystalline phase. Plasma nitriding is a non-equilibrium process that the active nitrogen atoms continuously bombard onto the surface of the target. According to a cascade effect, projectile ions non-crystalize in a local area [31]. The interstitial solid solution of nitrogen atoms induces serious lattice distortion, resulting in the formation of the metastable amorphous solid solution in a small local area on the top layer [32]. According to the thermodynamic model, spinodal decomposition takes place quickly during the nitriding process and thereafter, the nanocrystallization takes place [33].

3.2. Erosion-wear resistance behavior

The erosion-wear resistance behavior of the non-nitrided and nitrided samples was tested. The wear ratios of the substrate and the nitrided layer are shown in Fig. 5. The amounts of the projected particles are proportional to the wear depths for both substrates and nitrided layers. The slope calculated by linear fitting represents the erosion-wear ratio. The ordinate of the intersected point between the green and red line reveals the thickness of the nitrided layer. The ordinates of the intersected points in Fig. 5 are measured to be about 0.75, 5.2, 9.8, 11 and 13.4 μm, respectively, which well agrees with the cross-sectional morphology analysis. The value of the erosion-wear ratio of the sample nitrided at 673 K for 6 h is 0.183, which is smaller than that of the non-nitrided one (0.369), indicating that the erosion-wear resistance is doubly enhanced.

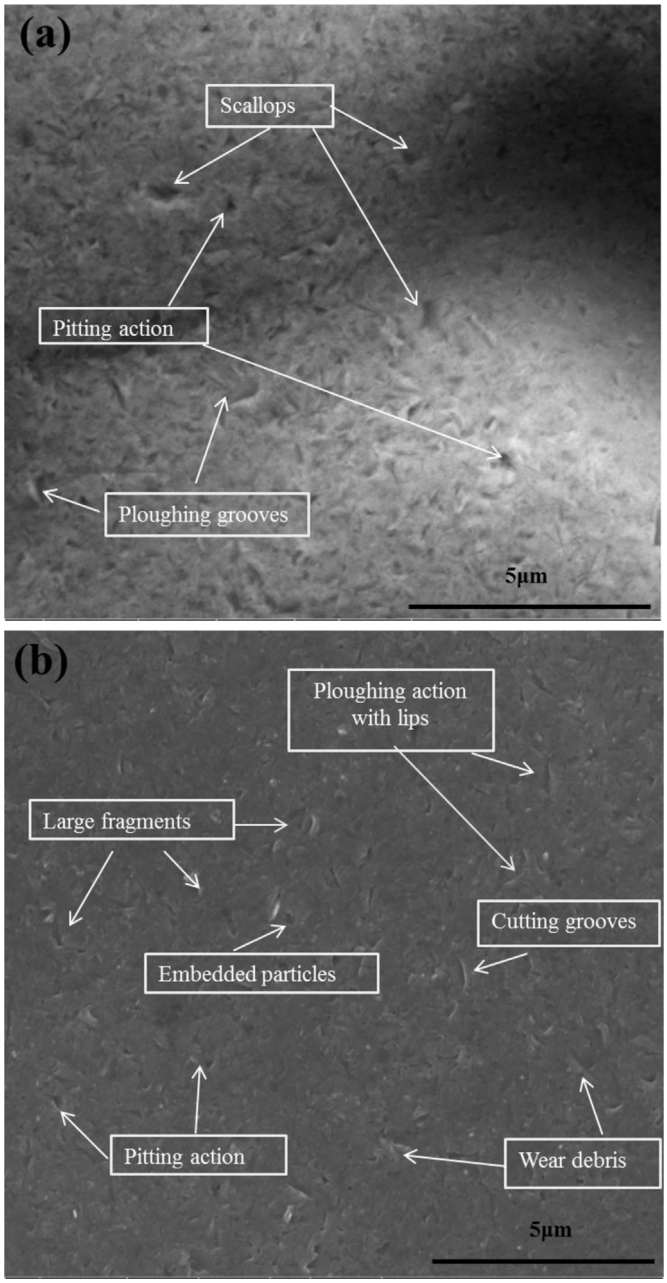

Fig. 6. SEM images of two different types of erosion damage at normal impact angle: (a) 673 K, 6 h and (b) 673 K, 18 h.

However, the erosion-wear ratios of the samples nitrided at 673 K for 18 and 24 h are 0.484 and 0.479, respectively, indicating that the erosion-wear resistance degenerates with a further increase of the nitriding time. The erosion-wear ratios of the samples nitrided at 673 K for 36 h and at 681 K for 18 h are 0.338 and 0.322, respectively, implying little change in erosion-wear resistance of these samples when compared to the non-nitrided sample.

The erosion-wear resistance behavior is related to the surface microhardness, microstructure, and compressive stress resulting from nitrogen interstitial solid solution induced lattice distortion [23,34]. Two different types of erosion mechanisms, namely, plastic deformation and brittle fracture, are identified based on the erosion damage morphology of the nitrided layer (Fig. 6). The predominant erosion damage of the non-nitrided sample at 90° is

brittle fracture, which is characterized by the high exfoliation of the large fragments on the surface [35]. Fig. 6a presents the erosion morphology of the sample nitrided at 673 K for 6 h, where a few erosion tracks and many erosion scallops are observed. This indicates that plastic deformation acts as the main erosion mechanism.

The decreased wear ratio under nitriding at 673 K for 6 h is generally attributed to the formation of γ_N phase, which is associated with the large compressive stress by the introduced nitrogen atoms that occupy the octahedral interstitial sites. Obvious signs of erosion damage such as ploughing action, pitting action, cutting grooves, embedded particles, large fragments, and wear debris are exhibited on the surface of the sample nitrided at 673 K for 18 h (Fig. 6b). As previously reported [23], the wear ratio of the nitrided samples decreased and the erosion-wear resistance was improved obviously. However, in this work, the wear ratio of the

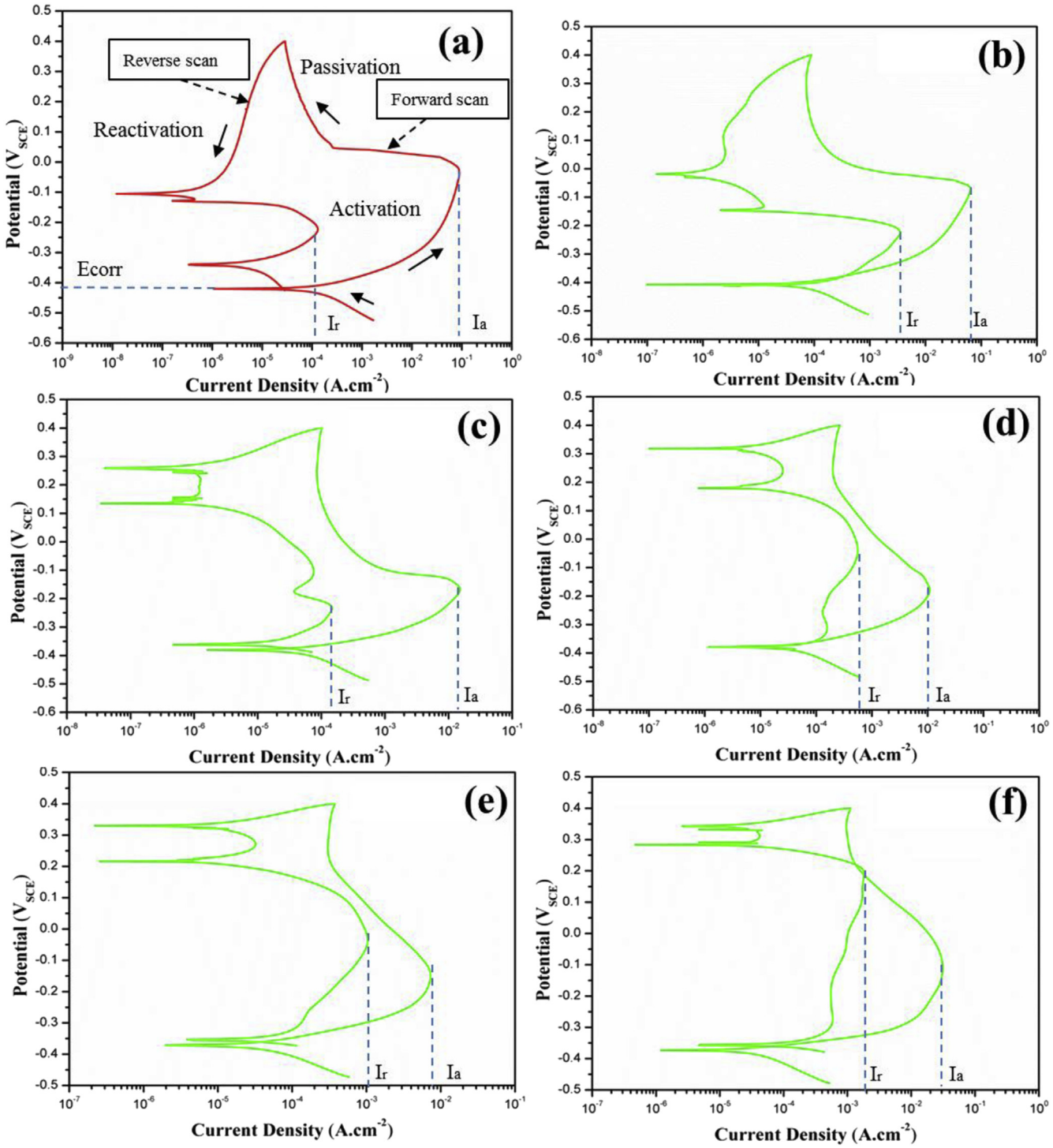

Fig. 7. DL-EPR curves of (a) the non-nitrided, (b) 673 K, 6 h (c) 673 K, 18 h, (d) 673 K, 24 h, (e) 673 K, 36 h and (f) 681 K, 6 h nitrided samples in a solution of 0.5 M H_2SO_4 + 0.01 M KSCN.

Table 2
The DOS values under different nitriding treatment temperatures and times by DL-EPR test.

Nitriding condition	Activation current I_a (A/cm^2)	Reactivation current I_r (A/cm^2)	DOS $R = I_r/I_a$
Non-nitrided	383.321×10^{-6}	0.560×10^{-6}	0.0015
673 K - 6 h	263.399×10^{-6}	13.685×10^{-6}	0.052
673 K - 18 h	64.800×10^{-6}	0.633×10^{-6}	0.0098
673 K - 24 h	46.846×10^{-6}	2.394×10^{-6}	0.051
673 K - 36 h	31.351×10^{-6}	4.460×10^{-6}	0.142
681 K - 18 h	142.146×10^{-6}	7.978×10^{-6}	0.056

sample nitrided at 673 K for 18 h increases. This is due to the formation of γ_N phase, nanocrystalline phase, and small amounts of Cr-nitrides. It indicates the synergistic presence of the two different types of erosion-wear mechanisms on the nitrided layer [36]. When further extending the nitriding time or increasing the nitriding temperature, the erosion-wear ratios of the samples decrease and finally are close to that of the non-nitrided sample (Fig. 5). This is attributed to the formation of large amounts of Cr-nitrides, nanocrystalline phase and lath-shaped structure, which can change the main erosion-wear mechanism from plastic deformation to brittle fracture. Notably, the erosion-wear resistance of the substrate after nitriding is improved because of the implantation of nitrogen atoms into the substrate.

3.3. Intergranular corrosion (IGC) resistance behavior

To reveal the effect of low-temperature plasma nitriding on the IGC resistance, the DL-EPR method is used to measure the DOS of IGC under different nitriding conditions. The DL-EPR curves and DOS values of the non-nitrided and nitrided samples are shown in Fig. 7 and Table 2. The maximum activation current (I_a) is generated when a passive film forms in the forward scan, This is attributed to the anode active dissolution on the surface of nitrided layer when the corrosion potential exceeds E_{corr}. The reduction of the I_a value occurs with the formation of the surface passivation film. In the region of passivation, a protective oxide film forms as a result of the reaction between the released metal ions from the sample surface and the dissolved oxygen. When the scan potential decreases to the active region during the inverse scanning process, the reactivation peak (I_r) appears with the breakdown of the protective film at the grain boundary. The formation of I_r results from the defective passive film of the chromium depleted regions in the anodic polarization process. Numerous reactivation peaks appear (Fig. 7) because of the formation of various phases on the surface after nitriding. A black and loose corrosion layer is observed on the surface of the samples. The corrosion layer can be easily peeled off, explaining the absence of metal luster on the surface of the sample (Fig. 8).

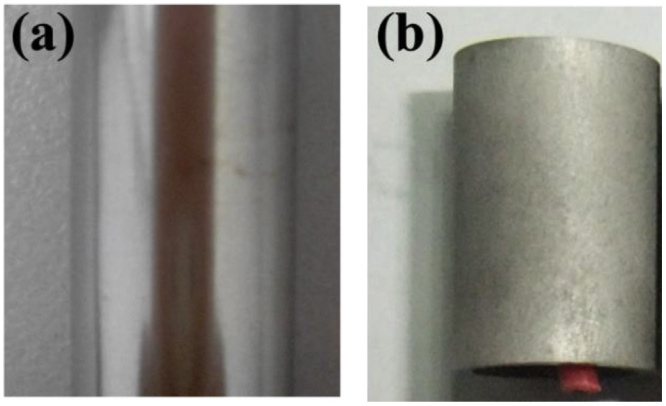

Fig. 8. Digital photographs of the non-nitrided sample: (a) without and (b) with DL-EPR test.

As shown in Fig. 7 and Table 2, the DOS values increase generally with the increase of the nitriding time, except for the sample nitrided at 673 K for 6 h (0.052). This sudden rise of the DOS is due to the existence of deleterious phases and uneven distribution of interface energy at the boundary under a short-time nitriding [37,38]. The I_r value reaches the maximum at 13.685×10^{-6} A/cm^2 for the sample nitrided at 673 K for 6 h. This phenomenon is possibly influenced by the distribution, morphology and balance of phases at the grain boundary, which results in the higher sensibility of IGC [39].

IGC prefers to attack the region of Cr-depletion and the solute segregation area at the grain or the phase boundary [40]. A significant increase of the DOS is related to the microstructure evolution and the new phase precipitation at the grain boundary. XRD and microstructure analysis indicate that Cr-nitrides (CrN and Cr_2N) form on the surface during plasma nitriding. The implanted N atoms react with Cr at the grain boundary and thereafter Cr-nitrides form on the interface. The precipitation of Cr-nitrides on the grain boundary results in low Cr components in the adjacent Cr depletion areas. Therefore, the grain boundary is more easily attacked when the Cr contents of the area adjacent to the Cr-nitrides are lower than the threshold values (approximate 12% Cr [41]) for the stainless steels [42]. Combined with HR-TEM results, the nanocrystalline phase generated on the surface after nitriding contributes to the significant increase of the DOS [37]. In contrast to the non-nitrided sample, the density of the grain boundary after the grain refinement is increased. Consequently, the length and network of the grain boundary after grain refinement are increased, which causes their strong attack [25].

4. Conclusions

(1) The microstructure and the precipitated phase before and after nitriding are investigated. The microhardness and the thickness of the nitrided layer are enhanced with the increase of the nitriding time. The values of the microhardness and the thickness reach as much as 1600 HK and 10 μm for the sample nitrided at 673 K for 36 h. The large enhancement of the surface microhardness is attributed to the formation of γ_N phase and Cr-nitrides (CrN and Cr_2N) on the nitrided layer. The amorphous and nanocrystalline phases are visible on the top of the nitrided layer. The nanoscale CrN phase is diffusely distributed in the γ_N regions.

(2) The erosion-wear resistance property of the non-nitrided and nitrided samples is studied in detail. The erosion-wear resistance of the sample nitrided at 673 K for 6 h is improved owing to a large compressive stress caused by the formation of the γ_N phase. The erosion-wear resistance degenerates when the nitriding time exceeds 6 h at 673 K.

(3) The DOS of IGC on the surface is obviously increased with the increase of the nitriding time, implying that the grain boundary of the samples is easily attacked after nitriding. The decrease of the IGC resistance of the nitrided samples is ascribed to the formation of Cr-depletion and re-crystallized nanoscale grains at the grain boundary.

Acknowledgments

We would like to acknowledge the financial support provided by the control rod cladding tube nitriding process study of State Nuclear Power Technology Corporation under Grant No.: SNP-KJ-CX-

2012-2, the National 973 Project of China (No. 2014CB046701). The authors gratefully thank Professor Volodymyr A. Yartys from Institute for Energy Technology, Norwegian University of Science&Technology and Dr. Xiao Zeng, Dr Zhigao Yi from Department of Chemistry, National University of Singapore for their constructive suggestions.

References

[1] T. Bell, Surf. Eng. 18 (2002) 453–458.
[2] Z.L. Zhang, T. Bell, Surf. Eng. 1 (1985) 131–136.
[3] Y. Sun, X.Y. Li, T. Bell, J. Mater. Sci. 34 (1999) 4793–4802.
[4] T. Czerwiec, N. Renevier, H. Michel, Surf. Coat. Technol. 131 (2000) 267–277.
[5] A.A.C. Recco, D. López, A.F. Bevilacqua, F. da Silva, A.P. Tschiptschin, Surf. Coat. Technol. 202 (2007) 993–997.
[6] J.F. dos Santos, C.M. Garzón, A.P. Tschiptschin, Mater. Sci. Eng. A 382 (2004) 378–386.
[7] C. Blawert, A. Weisheit, B.L. Mordike, F.M. Knoop, Surf. Coat. Technol. 85 (1996) 15–27.
[8] D.N. Wasnik, V. Kain, I. Samajdar, B. Verlinden, P.K. De, Acta Mater. 50 (2002) 4587–4601.
[9] S.X. Li, Y.N. He, S.R. Yu, P.Y. Zhang, Corros. Sci. 66 (2013) 211–216.
[10] M.Z. Yi, B.Y. Huang, J.W. He, Wear 252 (2002) 9–15.
[11] F.A.P. Fernandes, S.C. Heck, R.G. Pereira, C.A. Picon, P.A.P. Nascente, L.C. Casteletti, Surf. Coat. Technol. 204 (2010) 3087–3090.
[12] (a) B. Larisch, U. Brusky, H.J. Spies, Surf. Coat. Technol. 116–119 (1999) 205–211;
(b) E. Menthe, K.T. Rie, J.W. Schultze, S. Simson, Surf. Coat. Technol. 74–75 (1995) 412–416.
[13] L. Wang, J.C. Sun, X.L. Xu, Surf. Coat. Technol. 145 (2001) 31–37.
[14] M. Samandi, B.A. Sheddeen, D.I. Smith, G.A. Collins, R. Hutchings, J. Tendys, Surf. Coat. Technol. 59 (1993) 261–266.
[15] S. Adachi, N. Ueda, Thin Solid Films 523 (2012) 11–14.
[16] H.J. Kim, S.H. Jeon, S.T. Kim, I.S. Lee, Y.S. Park, K.T. Kim, Y.S. Kim, Corros. Sci. 87 (2014) 60–70.
[17] W.P. Tong, N.R. Tao, Z.B. Wang, J. Lu, K. Lu, Science 299 (2003) 686–688.
[18] J. Baranowskaa, S.E. Franklin, Wear 264 (2008) 899–903.
[19] R. Mohammadzadeh, A. Akbari, Mater. Charact. 93 (2014) 119–128.
[20] D. Manova, T. Höche, S. Mändl, H. Neumann, Nucl. Instrum. Methods Phys. Res. Sect. B 267 (2009) 1536–1539.
[21] J.A. Alegría-Ortega, L.M. Ocampo-Carmona, F.A. Suárez-Bustamante, J.J. Olaya-Flórez, Wear 290–291 (2012) 149–153.
[22] J. Flis, J. Mankouski, E. Rolinski, Surf. Eng. 5 (1989) 151–157.
[23] Y.T. Xi, D.X. Liu, D. Han, Appl. Surf. Sci. 254 (2008) 5953–5958.
[24] ASTM Standard G108-92, Standard Test Method for Electrochemical Reactivation (EPR) for Detecting Sensitization of AISI Type 304 and 304L Stainless Steels, ASTM, PA, 1993, pp. 457–465.
[25] S. Rahimi, D.L. Engelberg, T.J. Marrow, Corros. Sci. 53 (2011) 4213–4222.
[26] J.C. Stinville, C. Tromas, P. Villechaise, C. Templier, Scr. Mater. 64 (2011) 37–40.
[27] X.L. Xu, L. Wang, Z.W. Yu, Z.K. Hei, Surf. Coat. Technol. 132 (2000) 270–274.
[28] L. Wang, S.J. Ji, J.C. Sun, Surf. Coat. Technol. 200 (2006) 5067–5070.
[29] A. Toro, W.Z. Misiolek, A.P. Tschiptschin, Acta Mater. 51 (2003) 3363–3374.
[30] G. Miyamoto, A. Yonemoto, Y. Tanaka, T. Furuhara, T. Maki, Acta Mater. 54 (2006) 4771–4779.
[31] C.D. Yin, J.P. Zhang, Q. Gu, Z.J. Xu, J. Semicond. 8 (1987) 418–422.
[32] B. Schwarz, S.R. Meka, R.E. Schacherl, E. Bischoff, E.J. Mittemeijer, Acta Mater. 76 (2014) 394–403.
[33] A. Martinavicius, G. Abrasonis, A.C. Scheinost, R. Danoix, F. Danoix, J.C. Stinville, G. Talut, C. Templier, O. Liedke, S. Gemming, W. Moller, Acta Mater. 60 (2012) 4065–4076.
[34] L. Wang, B. Xu, Z.W. Yu, Y.Q. Shi, Surf. Coat. Technol. 130 (2000) 304–308.
[35] J.R. Laguna-Camacho, A. Marquina-Chávez, J.V. Méndez-Méndez, M. Vite-Torres, E.A. Gallardo-Hernández, Wear 301 (2013) 398–405.
[36] G.R. Desale, C.P. Paul, B.K. Gandhi, S.C. Jain, Wear 266 (2009) 975–987.
[37] M. Matulaa, L. Hyspecka, M. Svoboda, V. Vodarek, C. Dagbert, J. Galland, Z. Stonawska, L. Tuma, Mater. Charact. 46 (2001) 203–210.
[38] K.S. de Assis, A.C. Rocha, I.C.P. Margarit-Mattos, F.A.S. Serra, O.R. Mattos, Corros. Sci. 74 (2013) 250–255.
[39] F.E.A. Jouni, C.M. Sellars, Mater. Sci. Technol. 19 (2003) 1311–1320.
[40] C.T. Kwok, K.H. Lo, W.K. Chan, F.T. Cheng, H.C. Man, Corros. Sci. 53 (2011) 1581–1591.
[41] N. Parvathavarthini, Corrosion of Austenitic Stainless Steels: Mechanism, Mitigation and Monitoring, a Volume in Woodhead Publishing Series in Metals and Surface Engineering, 2002, pp. 117–138.
[42] N. Parvathavarthini, S. Mulki, R. K. Dayal, I. Samajdar, K. V. Mani, B. Raj, Sensitisation and testing for intergranular corrosion, in: H.S. Khatak, B. Raj(Eds.), Corrosion of Austenitic Stainless Steels. Mechanism Mitigation and Monitoring, Norasa Publishing House, New Delhi, 117–138.